Proton Sponge Lead Halides containing 1D polyoctahedral chains

Candida Pipitone,[a] Francesco Giannici,*[a] Antonino Martorana,[a] Federica Bertolotti,[b] Gabriele Calabrese,[c] Silvia Milita,[c] Antonietta Guagliardi,[d] Norberto Masciocchi*[b]

Received 00th January 20xx,
Accepted 00th January 20xx

DOI: 10.1039/x0xx00000x

Hybrid one-dimensional lead halides, containing the protonated 1,8-bis(dimethylamino)naphthalene moiety ($C_{14}H_{19}N_2$, monoprotonated "proton sponge"), were prepared by simple one-pot methods and investigated in terms of crystal structure, morphology, thermal stability and electronic properties. The as-precipitated $(C_{14}H_{19}N_2)PbBr_3$ and $(C_{14}H_{19}N_2)PbI_3$ species are isostructural and crystallize in the orthorhombic *Pbca* space group, resulting in 1D crystal phases with $([PbX_3]^-)_\infty$ chains (built by face-sharing $[PbX_6]$ octahedra; X = Br, I), among which the $(C_{14}H_{19}N_2)^+$ cations are inserted. The two compounds display complete miscibility in the solid state: both $(C_{14}H_{19}N_2)PbI_2Br$ and $(C_{14}H_{19}N_2)PbIBr_2$ crystal phases were successfully synthetized and do not show segregation effects. TGA and DSC measurements showed that, while all these materials are stable up to 250°C, the iodine-rich $(C_{14}H_{19}N_2)PbI_3$ and $(C_{14}H_{19}N_2)PbI_2Br$ species undergo an irreversible phase transition around 220 °C to a high-temperature phase, with a smaller molar volume and an apparent symmetry lowering (to orthorhombic $Pca2_1$). In these two cases, variable-temperature X-ray diffraction measurements showed a substantial crystal-to-crystal transformation, without intermediate melting or amorphization. The thermal expansion coefficients of $(C_{14}H_{19}N_2)PbI_3$ and $(C_{14}H_{19}N_2)PbBr_3$ are highly anisotropic and on the order of 10^{-4} K^{-1} along the **b** crystallographic axis. Microscopic and spectroscopic measurements were performed to complement the structural analysis of the samples: band gaps in the near UV range (3.3 and 3.8 eV for $(C_{14}H_{19}N_2)PbI_3$ and $(C_{14}H_{19}N_2)PbBr_3$, respectively) were obtained.

Introduction

In the last two decades, hybrid halide perovskites have attracted great attention as possible photovoltaic materials with a record efficiency of 25.2% in a solar cell device implementing a thin film of $((CH(NH_2)_2)PbI_3)_{0.95}$ $((CH_3NH_3)PbBr_3)_{0.05}$ [1-6]. Their appealing properties, such as high carrier mobility, tunable spectral absorption range, long diffusion lengths, low thermal conductivity, as well as the simplicity and affordability of fabrication,[7,8] make them good prospective candidates for other green-energy applications: for example, in solar thermoelectric[9,10] and optoelectronic[11,12] devices, light emitting diodes,[13,14] photodetectors[15,16] and lasers.[17]

So far, the most studied hybrid compounds are based on the three-dimensional perovskite structure ABX_3, formed by corner-sharing $[BX_6]$ octahedra, where B is a bivalent inorganic cation (*e.g.* Ge^{2+}, Sn^{2+} or Pb^{2+}), X is a halide (Cl^-, Br^-, I^-), and A is an organic monovalent cation [*e.g.* $CH_3NH_3^+$ (methylammonium, MA) or $[CH(NH_2)_2]^+$ (formamidinium, FA)], which can also be partially substituted by an inorganic one (Rb^+ or Cs^+),[18] located in the dodecahedral cavity formed by eight octahedra[19-21] However, even though hybrid perovskites have demonstrated promising transport, optical and thermal properties, their long-term stability is still a major concern in the development of working devices.[22,23]

In order to reach higher stability with enhanced properties, a large number of ABX_3 perovskites with different compositions have been studied in recent years. Despite of such efforts, it was soon realized that the 3D structures can only host a limited number of organic cations, as the cuboctahedral cavities of these perovskites are too small to accommodate ionic entities larger than MA or FA. The possibility of forming a 3D structure is mostly determined by spatial constraints, as summarized by Goldschmidt's Tolerance Factor (*TF*):

$$TF = \frac{(r_A + r_X)}{\sqrt{2}(r_B + r_X)} \qquad (1)$$

In equation 1, r_i are the ionic radii of A, B or X. It is generally found that for *TF* values 0.8–1, a 3D perovskite structure can be formed. Kieslich *et al*.[24] calculated the *TF* for over 2300 ABX_3 hybrid perovskites, based on the combinations of 14 small protonated amines for the A site, 21 divalent metals for B and 8 different anions for X. Of these, only 742 showed *TF*s between 0.8 and 1, and most compounds are not expected to show the same promising properties of the pristine $MAPbI_3$.

Another compositional study hypothesizes different structures relying on fixed A site and either partial or total substitution of B site,[25] but even in this case the number of promising compounds is still very limited. A different strategy could be playing with the structural dimensionality of available compounds to 2D, 1D and 0D structures, where layers of corner-linked octahedra (2D), chains of face-sharing octahedra (1D) and even isolated BX_6 octahedra (0D) are separated by large cationic spacers. In this way the possibility to choose larger cations increases drastically as the dimensionality decreases. These low-dimensional structures, and significantly lead halide derivatives, are easily prepared and have thin film processability as good as their 3D counterparts. They also display a proven enhanced stability and a more pronounced structural flexibility, which leaves more room to explore this

[a] *Dipartimento di Fisica e Chimica, Università di Palermo, viale delle Scienze, Ed. 17, 90128 Palermo (Italy).*
[b] *Dipartimento di Scienza e Alta Tecnologia e To.Sca.Lab., Università dell'Insubria, via Valleggio 11, 22100 Como (Italy).*
[c] *Istituto per la Microelettronica e Microsistemi, Consiglio Nazionale delle Ricerche, via Gobetti 101, 40129 Bologna (Italy).*
[d] *Istituto di Cristallografia e To.Sca.Lab., Consiglio Nazionale delle Ricerche, via Valleggio 11, 22100 Como (Italy)*

Electronic Supplementary Information (ESI) available: Elemental maps, Rietveld refinements of XRPD data, VTXRD, thermogravimetric and calorimetric curves. See DOI: 10.1039/x0xx00000x

class of compounds. Moreover, a wide(r) library of available organic cations can be inserted in the structures, since cations with larger size or even with higher charge may be used.[26,27] Therefore, exploiting different organic cations and inorganic chains is a viable strategy to significantly increase the chance of finding better performing compounds with tunable properties.

Highly performing photovoltaics, such as the cesium, methylammonium and formamidinium $APbI_3$ species, show rather complex phase diagrams, including the so-called 1D δ-phases: these are in some cases thermodynamically favored but also functionally silent,[28,29] even though this is not always true.[30] Recent reports on mixed 3D/1D composites,[31,32] where the "cubic" perovskite is coupled with a 1D system, showed enhanced stability and performances, rejuvenating the field of low-dimensional $APbI_3$ structures.[33]

In this work, we demonstrate the easy one-pot preparation of hybrid lead halides (HLH), based on the 1,8-bis(dimethylamino)naphthalene (proton sponge) moiety, namely the $(C_{14}H_{19}N_2)PbI_{3-x}Br_x$ species (x = 0–3), leading to 1D structures (hereafter, 1DHLHs). The choice of the $(C_{14}H_{19}N_2)^+$ cation, possessing nearly null tendency toward H^+ release (pK_a in water = 12.1) was intended to limit decomposition paths typical of ammonium and iminium cations, manifesting low environmental (e.g. moisture) and thermal stabilities.[34-36]

The single-halide $(C_{14}H_{19}N_2)PbX_3$ samples (labelled as α-phases) were synthetized by precipitation from a hot HX (X = I or Br) solution using PbO and $C_{14}H_{18}N_2$ as precursors. To test the miscibility of I and Br, two mixed samples with x = 1 or 2 were also synthetized by precipitation from hot DMF solution with $PbI_2/C_{14}H_{19}N_2Br$ and $PbBr_2/C_{14}H_{19}N_2I$ as precursors. They show complete solid-state miscibility, which can be used to tune the structural, thermal and functional properties of the compounds.

In the absence of single crystals of suitable size and quality, the crystal structure of these species was determined by *ab initio* X-ray Powder Diffraction (XRPD) and further investigated by variable-temperature XRPD (VT-XRPD) methods, which we used to estimate the thermal expansion coefficients of the samples. At room temperature, the four compounds are isomorphic and crystallize in the same space group (*Pbca*), with slightly different cell parameters. The x = 0 and x = 1 (I-rich) samples showed another phase at higher temperature as confirmed by calorimetry measurements. This new phase was found to be indefinitely stable at ambient conditions, structurally characterized and labelled hereafter as β-$(C_{14}H_{19}N_2)PbI_3$. The structural characterization of the 1DHLHs samples was further complemented by electron microscopy, and spectroscopic and thermal methods.

Experimental

Materials. Lead oxide (PbO, 99%), hydroiodic acid (aqueous HI, 57% w/w stabilized with 1.5 % w/w H_3PO_2) and hypophosphorous acid (H_3PO_2, 50% w/w aqueous solution) were used as received from Alfa Aesar. Lead bromide ($PbBr_2$, >98%), hydrobromic acid (HBr, ACS reagent 48%), hydrochloric acid (HCl, ACS reagent 38%), proton sponge ($C_{10}H_6(N(CH_3)_2)_2$, 99%), anhydrous ethanol (C_2H_6O, >99%) and dimethylformamide (C_3H_7NO, 98%) were purchased from Sigma-Aldrich. For the sake of conciseness, in the following the proton sponge is denoted as PRS, or as PRSH in its protonated form.

Lead iodide was prepared by dissolving PbO in aqueous HI solution and subsequent precipitation of PbI_2 through further H_2O addition. Solid (PRSH)Br and (PRSH)I salts were prepared by dissolving PRS in hot water, followed by the addition of an excess of HBr and HI, respectively, causing their quantitative precipitation.

Synthesis of $(PRSH)PbX_3$ (X = I, Br, Cl).

$(PRSH)PbI_3$ α-phase: PbO powder (3 mmol, 669 mg) was dissolved in 5 mL of aqueous HI and 1.7 mL of H_3PO_2. The solution was brought to 130 °C in order to dissolve all the lead oxide, resulting in a bright yellow solution. Solid PRS (3 mmol, 643 mg) was then added, causing the immediate precipitation of a yellow powder. The solution was left to cool to room temperature overnight. The honey-yellow polycrystalline material was collected by filtration under vacuum and washed with anhydrous ethanol. Yield 83%.

$(PRSH)PbI_3$ β-phase: 100 mg of *$(PRSH)PbI_3$* (α-phase) were placed in an alumina crucible and heated in an oven, in air, for 15 min at 220°C; after cooling to room temperature within minutes, the canary-yellow crystalline powder of the b-phase, indefinitely stable at ambient conditions, was quantitatively recovered. Yield: quantitative.

$(PRSH)PbBr_3$: PbO powder (3 mmol, 669 mg) was dissolved in 5 mL of aqueous HBr by heating the solution up to 130°C. Solid PRS (3 mmol, 643 mg) was then added, causing the immediate precipitation of a white powder. The solution was left to cool to room temperature overnight. The creamy-white polycrystalline material was collected by filtration under vacuum and washed with anhydrous ethanol. Yield 85%.

$(PRSH)PbCl_3$: The same reaction described above was conducted also in presence of aqueous HCl aiming at obtaining $(PRSH)PbCl_3$: this route however led to the precipitation of white $PbCl_2$ powder (XRPD evidences), without the formation of the sought hybrid 1DHLH chlorine-bearing species.

$(PRSH)PbI_2Br$ α-phase*:* PbI_2 powder (0.5 mmol, 230 mg) was dissolved in 2 mL of DMF by heating the solution up to 70°C. Solid (PRSH)Br (0.5 mmol, 148 mg) was then added. The solution was left to cool to room temperature overnight. Tiny white-pale yellow needles were collected by filtration under vacuum and dried in an oven at 60°C for 5h. Yield 50%.

$(PRSH)PbIBr_2$*:* $PbBr_2$ powder (1 mmol, 367 mg) was dissolved in 2 mL of DMF by heating the solution up to 70°C. Solid (PRSH)I (1 mmol, 342 mg) was then added. The solution was left to cool to room temperature overnight. White thin needles were collected by filtration under vacuum and dried in an oven at 60°C for 5h. Yield 54%.

$(PRSH)PbI_3$ thin film preparation*:* Solid $(PRSH)PbI_3$ was added to DMF (0.224 M); complete dissolution was achieved by vigorous stirring at 60 °C for 4 h. Thin films were deposited on a 20×15×1 mm (length × width × thickness) glass substrate by

spin coating using a hot (60 °C) DMF solution. The glass substrate was cleaned sequentially with soapy water, deionized water, acetone, and isopropyl alcohol in an ultrasonic bath for 10 minutes each. The substrate was then dried at 130 °C on a hot plate for 10 minutes. Five drops of the hot solution were directly cast on the substrate and then spin coated at 5000 rpm for 20 seconds.

Characterization.

Ab-initio crystal structure solution from laboratory X-ray diffraction data. XRPD data for structure solution of the (PRSH)PbI_3 (α and β-forms) and (PRSH)$PbBr_3$ phases were collected on a vertical scan q-q Bruker D8 Advance powder diffractometer equipped with a Lynxeye PSD detector in the 3–105° 2θ range, sampling at 0.02°, with scan time lasting approximately 16 h. Generator setting: 40 kV, 40 mA; fixed divergence slit: 0.5°; goniometer radius: 300 mm; sample holder for a flat specimen Bragg-Brentano parafocusing geometry: zero background silicon monocrystals, with a 0.2 mm deep cavity; Ni-filtered Cu-K_a radiation. Strong preferred orientation effects in (PRSH)$PbBr_3$ were limited by a small addition of Cab-O-Sil® (Sigma-Aldrich), an amorphous fumed silica powder granting a more random orientation of the crystallites. Standard peak search methods, followed by profile fitting, allowed the accurate estimate of the low-angle peak position, which, though the SVD indexing algorithm [37] implemented in TOPAS-R [38] provided primitive orthorhombic cells [a = 28.88, b = 18.13, c = 8.02 Å, GOF(20) = 44.2 for α-(PRSH)PbI_3; a = 24.98, b = 10.45, c = 8.00 Å, GOF(20) = 40.1 for β- (PRSH)PbI_3; and a = 28.05, b = 17.40, c = 7.88 Å, GOF(20) = 44.1, for (PRSH)$PbBr_3$]. Space group determination through the analysis of systematic absences indicated, for the three phases, *Pbca*, *Pca2$_1$* and *Pbca*, later confirmed by successful structure solution and refinement. Structure solutions were performed by Monte Carlo / Simulated Annealing technique using freely floating independent atom models for Pb and X atoms and a rigid model described by the Z-matrix formalism with standard geometrical parameters, for the PRSH molecule. The position of the N-H-N "bridging" hydrogen atom in PRSH, uninfluential to pattern simulation when X-rays (and not neutrons) are used, is here modelled in a nearly symmetrical mode, whereas, in the few neutron-base structure found in the Cambridge Structural Database H is preferentially bound to one N over the other. The final refinements were eventually carried out by the Rietveld method, maintaining the rigid bodies introduced at the structure solution stage. The background was modelled by a polynomial function of the Chebyshev type, peak profiles were described by the Fundamental Parameters Approach [39] and a common (refinable) isotropic thermal factor was attributed to all atoms. March-Dollase correction for preferred orientation [40] was applied in the form of g(*hkl*) and quoted below. Table 1 synoptically collects the crystal data and the pertinent Rietveld refinement agreement factors. Fractional atomic coordinates and crystal structure details were deposited with the CCDC (CSD Codes 2012750-2012752). These data can be obtained free of charge upon request from the Cambridge Crystallographic Data Centre via www.ccdc.cam.ac.uk /data_request/cif. A severe warning must be however set: as the organic core contains much lighter atoms than Pb, I and Br, and by observing that its overall disk shape has a nearly threefold symmetry (neglecting methyl groups), the absolute orientation of the PRSH cation might be poorly estimated. Starting from alternative orientations, several refinements have been carried out in parallel, leading to the "best performing" PRSH positioning as proposed in the final list of coordinates. For the mixed halide crystal phases, random distributions of the I/Br atoms over the octahedral sites was originally introduced, and additional tests carried out to check possible stereochemical preferences of smaller (larger) halides, as reported in classical perovskites. Variations of (restrained) site occupancy factors were also performed but a marginal improvement of the powder pattern matching agreement factors was observed, which we attribute to the increased number of free parameters. In this regard, we highlight that the 1D chain of face-sharing octahedra of our 1DHLHs have an ideal threefold symmetry (rod group p-6m2), making the halides "all equivalent", in that they are topologically indistinguishable, suggesting that preferential location may not take place.

Variable temperature XRD analysis. Thermodiffractometric experiments from 30 to 240 °C were performed on the two pristine α-(PRSH)PbI_3 and (PRSH)$PbBr_3$ phases, using the same diffractometer and optics (Bruker D8 Advance) illustrated for XRPD structural analysis data collection. Powdered batches were deposited in the hollow of an aluminum sample holder of a custom-made heating stage, assembled by Officina Elettrotecnica di Tenno, Ponte Arche, Italy; diffractograms were acquired in air, in the most significant low-angle 2θ ranges (5-25° 2θ). Since in powder diffraction experiments the samples are in direct contact with the air and some thermal drifts/gradients are present, the accurate phase transition temperatures are taken from DSC measurements. All the diffraction data shown in the manuscript were collected in flat-plate Bragg-Brentano symmetrical geometry: this applies to both room-temperature and temperature-resolved XRPD measurements.

Thermal analyses (TG and DSC): Thermogravimetric (TG) curves from 30 to 700°C (5 °C min^{-1}) were acquired using a TA Q5000 thermogravimetric analyzer (TA Instruments) under a nitrogen flow on a platinum sample holder. Differential scanning calorimetry (DSC) curves from 25°C to 280°C (heating/cooling rate 25 °C min^{-1}) were acquired using a DSC 2920 differential scanning calorimeter (TA Instruments) under a nitrogen flow on a sealed Al pan.

Scanning electron microscopy (SEM). SEM micrographs in secondary-electron mode were collected with a FEI Versa 3D microscope equipped with a Bruker Quantax energy-dispersive fluorescence analyzer using a 10 kV acceleration voltage.

Infrared spectroscopy. IR spectra were recorded in the 400 to 4000 cm^{-1} spectral range using a Perkin Elmer Frontier FT-IR spectrometer. The samples were dispersed in KBr and pressed into 13 mm Ø pellets using a 10 tons hydraulic press.

Table 1. Crystal data for the five species characterized by powder diffraction methods.

Species	α-(PRSH)PbI_3	(PRSH)PbI_2Br	(PRSH)$PbIBr_2$	(PRSH)$PbBr_3$	β-(PRSH)PbI_3
Formula	$C_{14}H_{19}N_2I_3Pb$	$C_{14}H_{19}BrI_2N_2Pb$	$C_{14}H_{19}Br_2IN_2Pb$	$C_{14}H_{19}Br_3N_2Pb$	$C_{14}H_{19}N_2I_3Pb$
fw, g mol^{-1}	803.23	756.23	709.23	662.23	803.23
System	orthorhombic	orthorhombic	orthorhombic	orthorhombic	orthorhombic
Space group	*Pbca*	*Pbca*	*Pbca*	*Pbca*	*$Pca2_1$*
a, Å	28.8862(4)	28.4148(9)	27.9436(7)	28.0408(6)	25.053(1)
b, Å	18.1330(2)	18.0671(6),	17.8058(4)	17.3850(4),	10.4016(5)
c, Å	8.0262(1)	7.9645(2)	7.8986(4)	7.8858(2)	8.0082(2)
V, $Å^3$	4204.1(1)	4088.8(2)	3930.0(2)	3844.2(2)	2086.9(2)
Z	8	8	8	8	4
ρ_{calc}, g cm^{-3}	2.538	2.457	2.397	2.288	2.556
μ(Cu K_α),cm^{-1}	496.1	414.7	332.2	238.1	499.7
(hkl), g	(010), 0.93	(001), 0.89	(001), 1.20	(001), 0.97	(001), 0.97
R_p , R_{wp},	0.071, 0.099	0.071, 0.095	0.087, 0.112	0.067, 0.094	0.070, 0.102
R_{Bragg}	0.060	0.089	0.076	0.069	0.069
2θ range, °	5-105	5-105	5-105	5-105	5-105

UV-vis-NIR spectroscopy. UV-vis-NIR spectroscopy. UV-vis-NIR reflectance spectra were measured in the 200 – 2500 nm range using a modular USB 2000 + XR spectrometer equipped with DH-mini UV-vis-NIR light source by Ocean Optics. $BaSO_4$ was used as reflectance standard and the measurements were performed on pelletized powders. The Kubelka-Munk function F[R] was calculated from reflectance spectrum R(E), where E is the photon energy, using the $F[R] = (1-R)^2/2R$ relationship.[41] Taking F[R] as representative of the sample absorbance spectrum, extrapolation of the linear portion of the $(F[R]*E)^2$ *vs*. E plot on the E axis provided experimentally accessible *direct band gap* values.

X-Ray Fluorescence Spectroscopy. Gently ground powders of the mixed-halide α-(PRSH)PbI_2Br and (PRSH)$PbIBr_2$ phases were deposited on a polycarbonate film within a Minipal XRF Spectrometer (Panalytical), equipped with a Cr-anode operated at 30 kV and 3 μA. X-ray fluorescence lines were measured for I (multiple L lines at in the 3.9-4.5 keV range) and Br (Kα/β doublet at 11.9/13.3 keV).

Phase stability upon exposure to Laser light. Gently ground powders of the mixed-halides (α-(PRSH)PbI_2Br and (PRSH)$PbIBr_2$) phases were deposited on a quartz monocrystal and illuminated by blue laser (λ = 405 nm, 40 mW) for 10 hours. XRPD spectra collected before and after illumination were identical.

Results and discussion

Composition and morphology. The 1DHLHs precipitated from aqueous HX solutions and investigated in the present work are exceptionally pure, if compared with the products obtained from other methods.[21] For α-(PRSH)PbI_3 and (PRSH)$PbBr_3$, high yields (well above 80%) are also obtained. For the iodine derivative, immediately after the addition of PRS powder, the clear yellow solution became really dense, to the point that magnetic stirring was not able to maintain the homogeneity of the resulting suspension, and sonication was briefly used. SEM imaging of both samples (see Figure 1a,b) revealed crystal habits of prismatic shapes, in line with the orthorhombic crystal structure determined by XRPD, and discussed in the following section. While the size distribution of crystals in (PRSH)$PbBr_3$ appears to be relatively narrow (most crystallites have comparable sizes, falling in the 10-30 μm range), in α-(PRSH)PbI_3 a relevant fraction of smaller crystals is also observed, possibly due to sonication and the increase of nucleation sites derived therefrom.

As mixed-halides systems have been often reported to form in lead halide perovskites and their analogs, we carried out also alternative syntheses mixing different precursors, of nominal 2:1 or 1:2 I/Br ratios, their products being labeled as α-(PRSH)PbI_2Br and (PRSH)$PbIBr_2$. SEM micrographs of the mixed halide samples unexpectedly displayed elongated (needle-like) crystal habits, heavily branched, with lengths up to around 500 mm. This morphology is likely the result of the different reaction media used during the synthesis (DMF vs. HX/H_2O). We tested this hypothesis by dissolving and recrystallizing (PRSH)PbI_3 and (PRSH)$PbBr_3$ powders in DMF. The resulting crystals showed the same crystal habit of the mixed compositions; this is tentatively attributed to direct solvent effects, with DMF inhibiting the crystal growth along specific directions, or even to the formation of intermediate (but undetected) solid phases containing DMF in their crystal structures, which then retain the observed needle-like shape even after the elimination of DMF by heating, as previously reported for $MAPbI_3$.[42,43]

Semiquantitative element ratio derived from EDX analysis confirmed the proposed stoichiometry for the x = 0 – 3 samples. Elemental ratios were also derived by quantitative XRF analyses performed on gently ground bulk materials, which ended up with $I_{0.72}Br_{0.28}$ and $I_{0.30}Br_{0.70}$ values for the two mixed phases of 2:1 and 1:2 (I:Br) nominal composition (estimated errors below 3%). The possibility of an uneven distribution of the anions in the mixed-halide samples [α-(PRSH)PbI_2Br and (PRSH)$PbIBr_2$] was investigated by XRPD and

EDX elemental mapping. The latter, shown in Figure 2 and Figure S1, clearly manifests a homogenous distribution, at the micrometer scale, of I and Br all over the sample. XRPD patterns of all compounds (single and mixed-halides) in Figure 3, show unsplit peaks of comparable width. This evidence confirms unequivocally the occurrence of truly monophasic crystal phases and indicate that no segregation effects are at work, therefore suggesting that anionic replacements are likely randomly distributed. Cell determination and refinement of the four isomorphous phases of nominal (PRSH)$PbI_{3-x}Br_x$ formulation (x = 0, 1, 2, 3), provided the relative changes of axial lengths and molar volumes, their trend with increasing x being shown in Figure 4, later illustrated. Significantly, the linear trend of the molar volumes vs. Br content (black triangles in Figure 4) confirms that the nominal stoichiometry reasonably matches the real one, with additivity of atomic volumes.

Crystallochemical analysis.

The end members (α-phases). The structures of the isomorphous α-(PRSH)PbI_3 and (PRSH)$PbBr_3$ crystal phases contain infinite one dimensional chains of $([PbX_3]^-)_\infty$ formulation, built by face-sharing $[PbX_6]$ octahedra and running parallel to the **c** axis, among which the organic molecules (interlocked along **b**, *vide infra*) are placed. Their crystal packing diagrams are shown in Figure 5. Table 2 synoptically collects the most relevant geometrical parameters for these species and for the other ones, later discussed in this section.

In the two α-phases, the polyanionic lead-halide chains are topologically identical but, as expected for the different size of the iodide and bromide ions (2.06 and 1.82 Å crystal radius, respectively[44]), they show different bond lengths (see Table 2): the average values are 3.26 Å and 3.06 Å for the Pb-I and Pb-Br bonds, respectively. In (PRSH)$PbBr_3$, thanks to the significant shrinking of the Pb-Br-Pb angles (average values: 75.8° *vs.* 79.9° in α-(PRSH)PbI_3), the non-bonding Pb···Pb interaction along the 1D chain (3.94 Å) is only marginally shorter than in the α-(PRSH)PbI_3 (4.01 Å). Accordingly, the length of the **c** axis contracts by a mere 2% within the entire set of the (PRSH)$PbI_{3-x}Br_x$ (x = 0 – 3) compositions (see Figure 4).

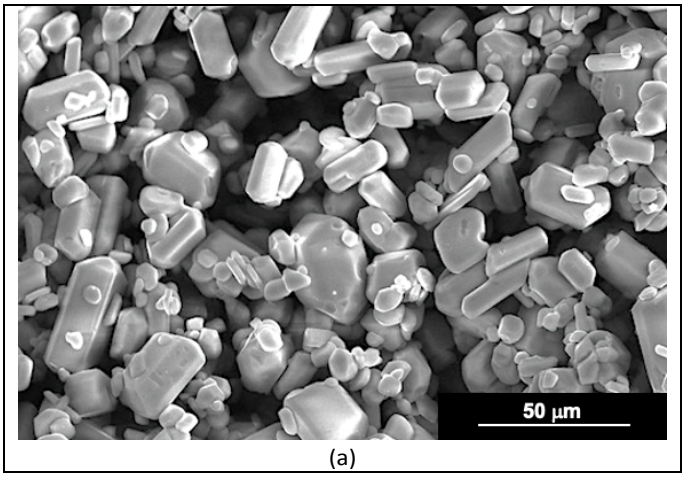

(a)

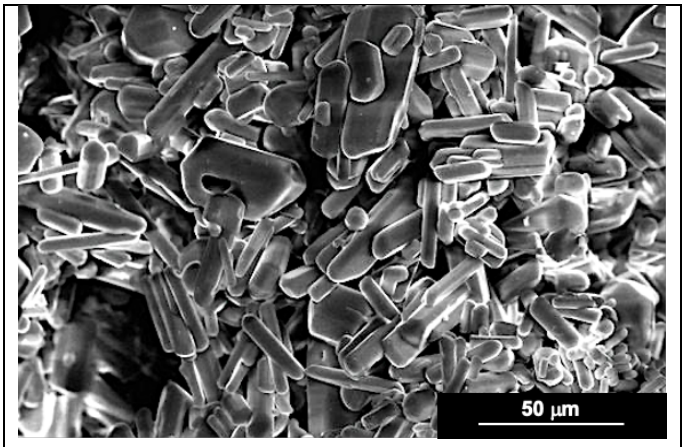

(b)

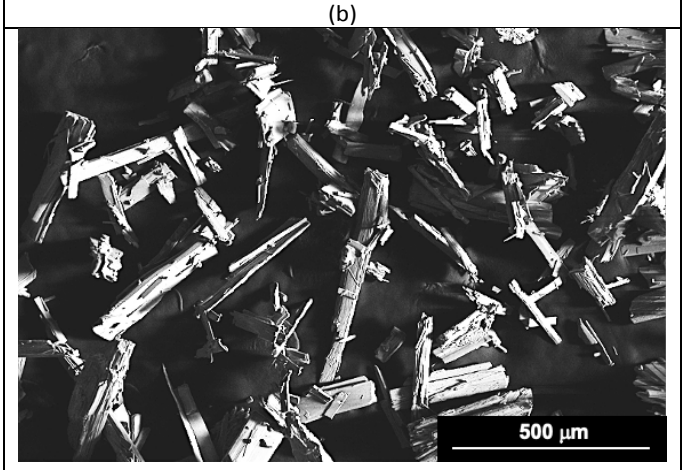

(c)

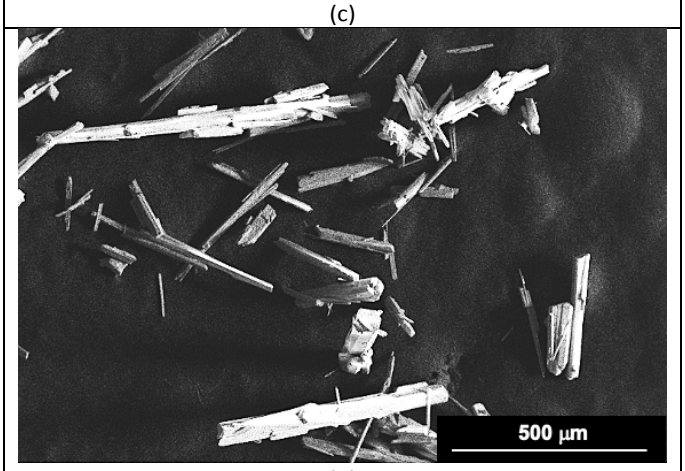

(d)

Fig. 1. SEM micrographs of α-(PRSH)PbI_3 (a), (PRSH)$PbBr_3$ (b), α-(PRSH)PbI_2Br (c) and (PRSH)$PbIBr_2$ (d). Note the very large aspect ratio of the crystals of the mixed halide species in (c) and (d), significantly different from those of the end members in (a) and (b). X-ray powder diffraction data of pristine and ground materials enabled to detect the orientation of the morphological long axis, found to be parallel to the structural **c** axis (in accordance to crystal morphology simulation by the BFDH model).

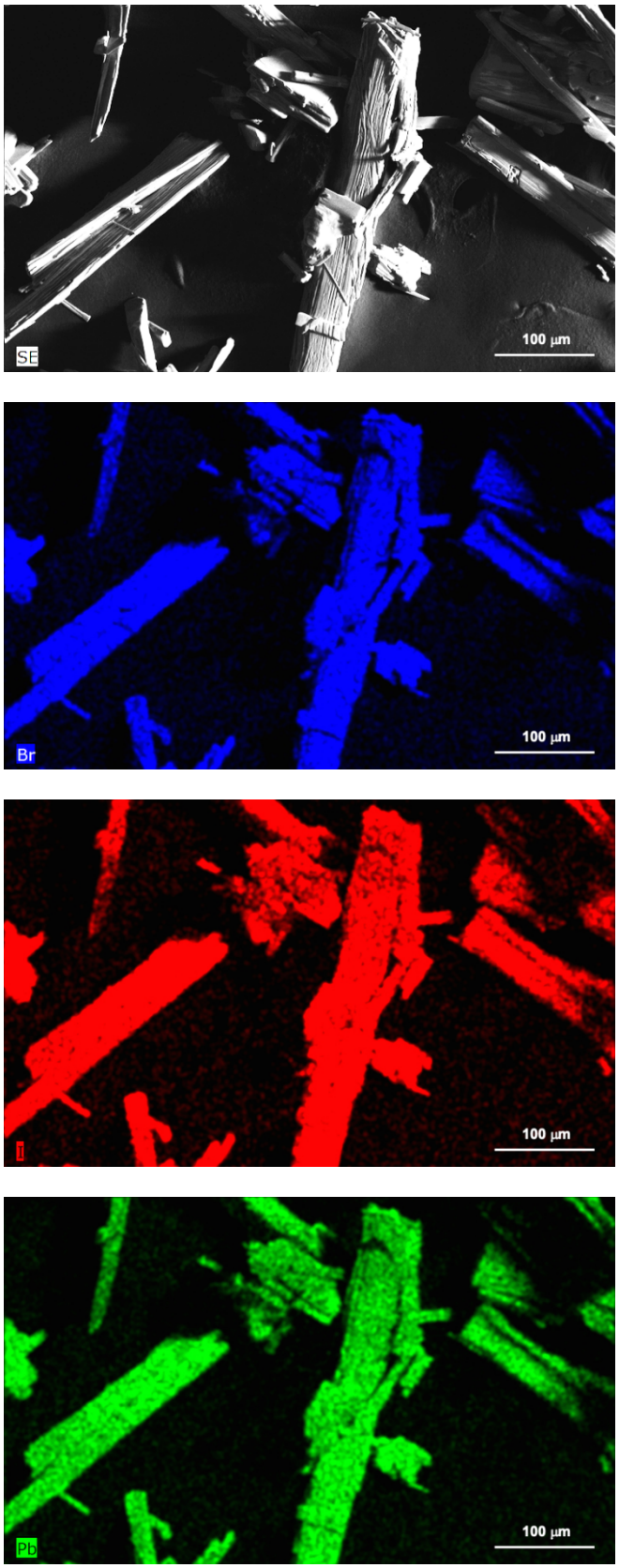

Fig. 2. EDX elemental maps of (PRSH)PbI_2Br: Bromine in blue, iodine in red and lead in green. Scale bar is 100 µm.

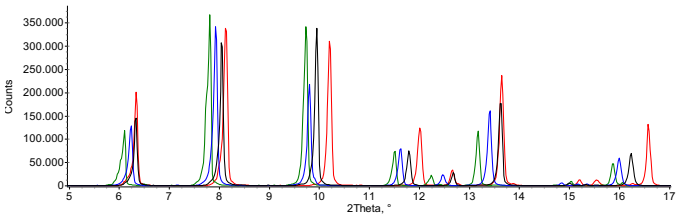

Fig. 3. Characteristic low-angle peaks (5-17° 2θ) for the α-(PRSH)$PbI_{3-x}Br_x$ crystal phases (x = 0, 1, 2, 3), where the shifts in angular position are the consequence of the slightly different lattice parameters. x = 0 in green, x = 1 in blue, x = 2 in black and x = 3 in red.

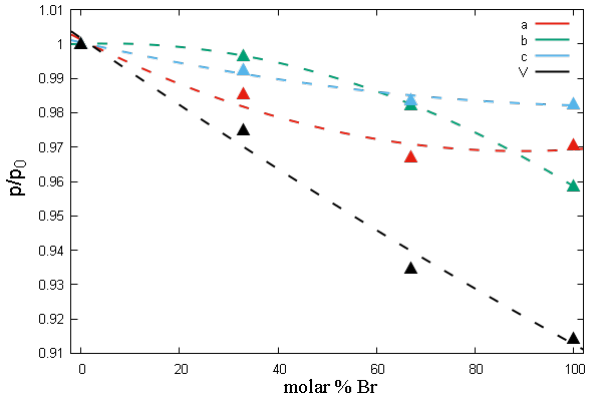

Fig. 4. Plot of the lattice parameters and volume variations (p_i values, *i* = a,b,c,V) for (PRSH)$PbI_{3-x}Br_x$ (x=0, 1, 2 and 3), with respect to (PRSH)PbI_3 (p_{i0}), *vs* Br/(Br+I) molar fraction. Relative (and dimensionless) p_i/p_{i0} values are plotted as solid triangles, parabolic fits are provided as a guide for the eyes. Uncertainties σ of the p/p_0 values (as provided by l.s. full pattern refinement on powder diffraction data) are smaller than the symbols (σ_p/p well below 10^{-4}, see Table 1).

Table 2. Synoptic collection of relevant (room temperature) structural parameters for the crystal structures reported in this paper. CSD2020 refers to the purely organic cation subset of the face-sharing $([PbI_3]^-)_\infty$ polymers found in the Cambridge Structure Database, 2020 edition (mean and standard deviation of the pertinent distribution).

Parameter	α-(PRSH)PbI_3[a]	β-(PRSH)PbI_3	CSD	(PRSH)$PbBr_3$
Pb···Pb, Å	4.01	4.01	4.04(11)	3.94
Pb–X1, Å	3.21; 3.34	3.23; 3.26		2.98; 3.15
Pb–X2, Å	3.20; 3.28	3.27; 3.27		2.93; 3.10
Pb–X3, Å	3.21; 3.34	3.19; 3.23		2.91; 3.33
<Pb–X> and spread, Å	3.26; *0.06*[b]	3.24; *0.03*[b]	3.24(7)	3.07; 0.16
Pb–Xn–Pb, °	X1: 75.6 X2: 76.5 X3: 75.4	X1: 76.2 X2: 75.6 X3. 77.2		X1: 80.0 X2: 81.6 X3 78.1
<Pb–X–Pb> and spread, °	75.8; 0.6	76.3; 0.8	77.0(2.1)	79.9; 1.8

[a] Statistically derived e.s.d's from XRPD data are < 0.02 Å for Pb-X bond distances and ~ 0.3° for Pb-X-Pb angles.
[b] Italicized values for the spread of the Pb-I distances are discussed in the text.

The 1D $([PbX_3]^-)_\infty$ chain structure and the way it packs are somewhat reminiscent of a simpler analogue, the (1-naphthylammonium)triiodoplumbate crystal phase, which shares the same space group symmetry (*Pbca*) and shows (after a legitimate permutation) similar cell parameters. Its geometrical parameters, to be compared with those reported in Table 2 for α-(PRSH)PbI_3 are: Pb···Pb = 3.95 Å, <Pb-I> = 3.22 Å and <Pb-I-Pb> = 75.6°.[45]

DSC measurements (see Figure 6) were performed on both a-(PRSH)PbI_3 and (PRSH)$PbBr_3$ materials to verify the presence of high temperature phases: α-(PRSH)PbI_3 shows a small endotherm (onset at 213°C, ΔH = +3.9 kJ mol^{-1}), attributed to the polymorphic α → β phase transition (also evidenced by VTXRD), while (PRSH)$PbBr_3$ does not show any feature in the DSC trace up to decomposition, occurring near 270 °C. Interestingly, β-(PRSH)PbI_3, discussed hereafter, does not convert back to the a-phase upon cooling (for kinetic reasons, see below), thus enabling its full structural XRPD characterization at ambient conditions.

The β-(PRSH)PbI_3 phase: Also the structure of b-(PRSH)PbI_3 is based on infinite chains of $([PbX_3]^-)_\infty$ formulation with Pb(II) ions octahedrally coordinated by μ_2-bridging iodides. The PRSH cations fill the interchain space (see Figure 5b) and mutually interact through non-polar C···H and H···H contacts along **b**, the details of which are not accessible by XRPD modeling.

As proven by DSC measurements (see above), the enthalpic content of the β-(PRSH)PbI_3 is higher than in α-(PRSH)PbI_3, implying a lower (more negative) enthalpy of formation for the a-phase, the thermodynamically-favored polymorph at 0 K (within an enantiotropic polymorphic system). As the molar volume of the β-(PRSH)PbI_3 phase (522.7 $Å^3$) is slightly smaller than in the α-phase (525.5 $Å^3$), the opposite conclusion should have been drawn by following the well-known "density rule".[46] The rule, however, has been essentially dismissed in a very recent study, though applied to monotropic systems only.[47] If equilibrium is assumed at the α → β onset temperature, then an entropic (temperature dependent) stabilization contribution, $\Delta S = \Delta H/T$ = +8.0 J mol^{-1} K^{-1}, for the high temperature formation of the β-phase must be invoked.

Additionally, the heat-induced centrosymmetric (*Pbca*) to non-centrosymmetric (*Pca2₁*) space group phase transformation involves an unexpected symmetry lowering. In this regard, a general consensus exists that the symmetry of matter generally (though not univocally[48,49]) increases upon raising the temperature, an effect mostly attributed to pathways governed by anharmonic vibrations and anisotropic thermal expansion.[50] This makes our observation somewhat counterintuitive. Local symmetry lowering, attributed to the presence of anharmonicity of atomic movements, thermally induced at high temperatures, have been claimed to occur in Pb-based binary semiconductors (marked as *emphanisis*[51]). However, this is likely not the mechanism leading to the phase transformation to *Pca2₁* In the case of the present work, the symmetry lowering is only *apparent.* Indeed, considering that both (*Pbca* and *Pca2₁*) structures have Z'=1 (Z' being the number of molecules in the asymmetric unit) and that the length of the **b** axis is nearly halved in the β-phase, the heat-induced transformation maintains the "complexity" of the system, the lower number of space-group symmetry elements in β-phase being counterbalanced by an increased translational symmetry. Worth to mention, in the clear absence of external polar forces inducing loss of inversion centers, the α → β (like any centrosymmetric to non-centrosymmetric) transformation must generate (poly)twinned crystallites with large enough domains not amenable to statistical disorder modeling. As symmetry is added to the crystal by twinning, an additional "disordering" term must be added, which makes the reported α → β an entropy driven transformation (with small, but positive, ΔS). Positive ΔH and ΔS variations speak for an enantiotropic polymorphic α → β phase transformation. Although enantiotropically-related polymorphic transitions are thermodynamically reversible with temperature and pressure, they may be observed as either reversible or irreversible in practical investigations. This behavior may be explained simply by a difference in the energy barrier for the transition and is particularly true for reconstructive (as in our case) rather than for displacive phase transformations. Therefore, the reconstructive nature of the observed α → β transformation is in line with a kinetically suppressed back-transformation and confirms the entropy-driven nature of the system.

As a further comment in favor of the acentric nature of the b phase, lattice metrics and density considerations indicate that Z value equals 4. In the orthorhombic crystal system, this value can be achieved in two ways: 1) the PRSH moiety (of idealized local *mm2* symmetry) being bisected by a crystal symmetry element of a centrosymmetric space group; 2) an acentric space group. The former case is easily dismissed since none of the plausible orientations of the organic cations matches the x (or y, or z) axis directions, as requested by a centrosymmetric space group. Possible disordering of the PRSH fragment compatible with centrosymmetry is also discarded: it does not lead to a satisfactory powder pattern matching, whereas adoption of the acentric *Pca2₁* space group fulfills the observed systematic absences pattern.

The non-bonding Pb···Pb distance in β-(PRSH)PbI_3 virtually matches that of the α-phase (see Table 2), as also the average Pb-I and Pb-I-Pb bond distance and angle do. Given that the organic cation is fairly rigid and does not possess flexible links (beyond methyl rotations about the C–N axis, possibly bearing low stereochemical significance), we tentatively attribute the larger entropy of the β-phase to the additional freedom associated to subtle packing effects (and to vibrational ones derivable therefrom), which are not detected by the limited real space resolution provided by XRPD. Nevertheless, one can further attribute the slight entropy increase in β-(PRSH)PbI_3 to the presence of much more homogeneous Pb-I distances (than in the α-phase), as witnessed by the evident reduction of their spread (italicized items in Table 2).

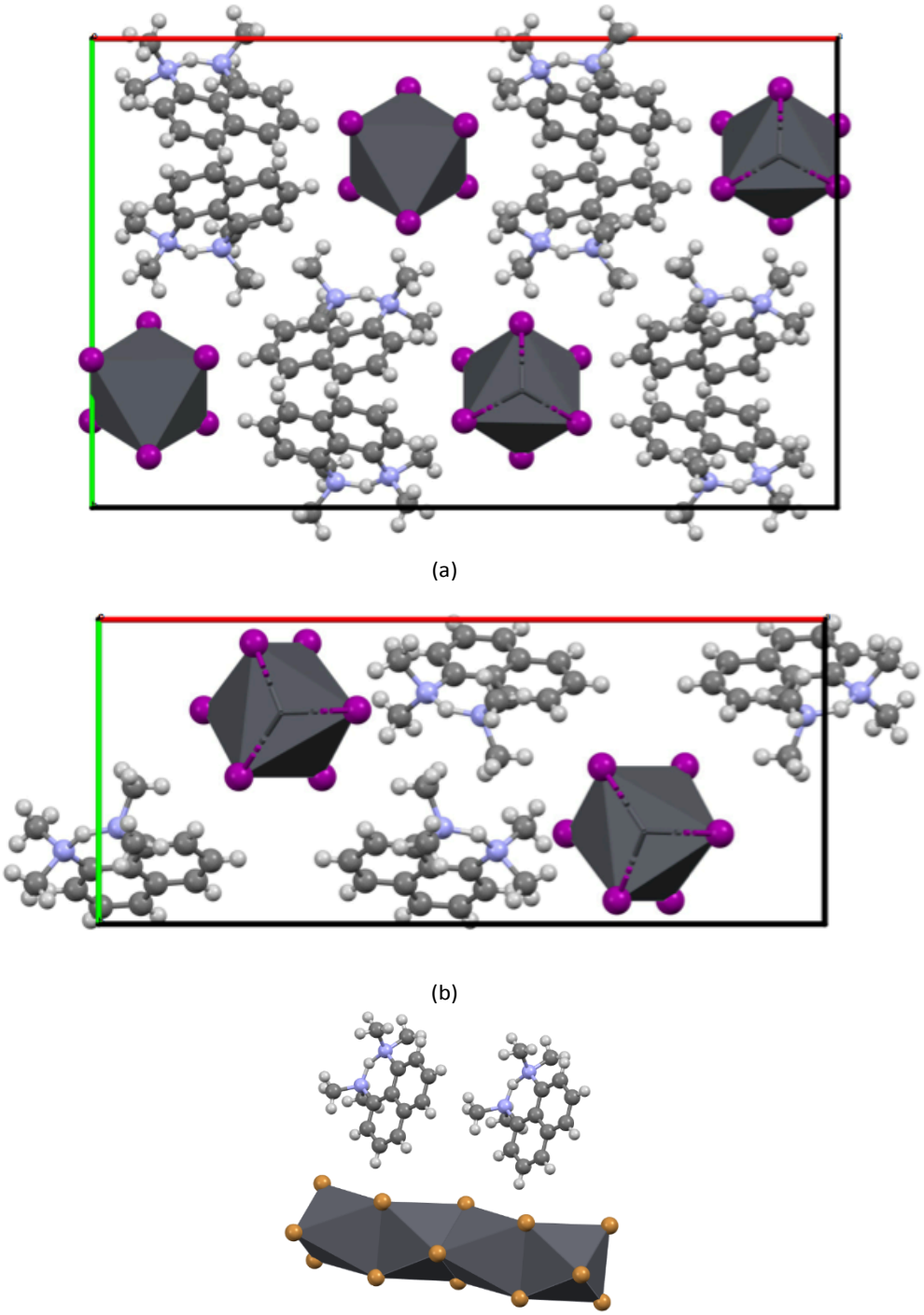

Fig. 5. Crystal structures of α-(PRSH)PbI_3 (a) and β-(PRSH)PbI_3 (b) imaged down the shortest axis (**c**, i.e. along the [001] chain direction of $([PbI_3]^-)_\infty$ formulation). Horizontal axis = **a** (in red); vertical axis = **b** (in green). Atom color code: C, black; H, white; N, blue and I, violet. Pb atoms are hidden within the polyoctahedral anions. At the drawing resolution the crystal structure of (PRSH)$PbBr_3$ is identical (with slightly smaller lattice parameters) to that shown in (a). In panel (c), a sketch of the polyhedral sequence along **c** within (PRSH)$PbBr_3$, shown approximately down **b.**

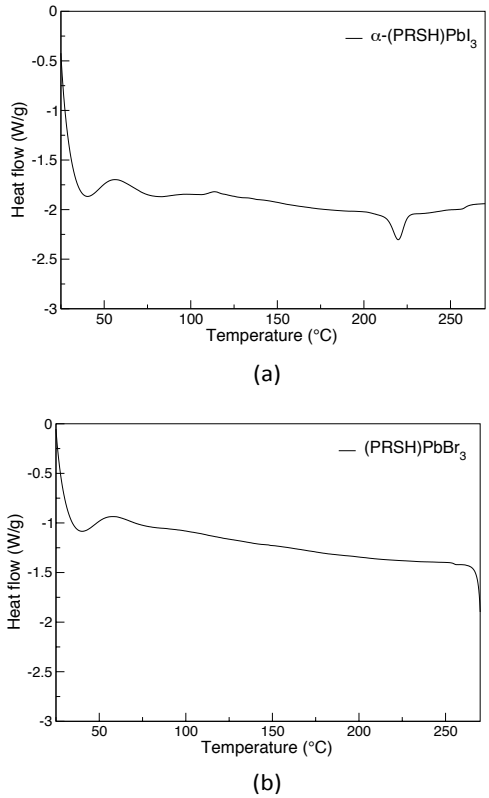

Fig. 6. Plots of the DSC traces of α-(PRSH)PbI_3 (a) and (PRSH)$PbBr_3$ (b). The weak endotherm (ΔH = +3.9 kJ mol^{-1}) at ca 220° in the former is attributed to the quantitative phase transformation into the β phase. The broad features observed at ca. 60°C was proved to be an instrumental artifact.

The (Z-normalized) unit cells of the two (PRSH)PbI_3 polymorphs can be compared as if they were one the deformation of the other. The metrics of such a deformation of the lattice can be elegantly represented by the so-called strain tensor, and its graphical representations. Using Ohashi's approach[52] and Kaminski's plotting routines[53], the variations of the lattice parameters from the α- to the β- phase of (PRSH)PbI_3, and between the isomorphous (PRSH)PbX_3 (X = I, Br) crystal structures were computed. The related tensor isosurfaces are drawn in Figure 7.

From the graphics shown in panel (a), one can easily appreciate that the vanishing component of the deformation tensor along *z* is a direct consequence of the constancy of the polyanionic chain periodicity upon moving from one polymorph to the other. On the contrary, in the *xy* plane, the differently colored *x* and *y* lobes indicate anticorrelated variations, since molar volumes nearly coincide. These observations clearly indicate that the 2D α and β lattices in **ab**, related to the relative disposition of the parallel $([PbX_3]^-)_\infty$ bundles, are markedly different, and much closer to a 2D hexagonal packing in the β-phase.

On the other hand, panel (b) shows a convex shape: this refers to the slightly anisotropic shrinking of the lattice parameters from the α-(PRSH)PbI_3 phase to the fully brominated isomorphous counterpart. Again, the lowest variation is observed along *z* (aligned with the 1D $([PbX_3]^-)_\infty$ chains running parallel to the crystallographic **c** axis), which remains the stiffer direction in the crystals.

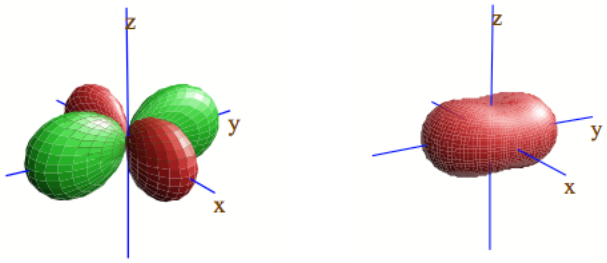

Figure 7. Plots of the deformation tensors related to the α-(PRSH)PbI_3 to β-(PRSH)PbI_3 transformation (a) and to the α-(PRSH)PbI_3 to (PRSH)$PbBr_3$ cell parameters changes (b). Expansion in green and contraction in red. The two panels are not to scale.

Interestingly, the cell parameters and volume changes in the isomorphous x = 0 – 3 series, graphically anticipated in Figure 4, show an approximate linear trend of the molar volume, in agreement with Zen's variation of Vegard's law.[54] This is less valid for the individual axes, likely manifesting preferential location, and orientation, of the PRSH cations (but not phase segregation), which is not visible in the standard Rietveld-Bragg's approach. In search for possible explanations of the anisotropic, and differential, behaviour of cell axes contraction upon increasing the Br molar content, we have checked the relative orientations of the octahedra within the different a-phases (I to Br), in terms of 1D chain rotations about **c**. Upon defining a ϕ_n angle (n=1,2,3) which addresses the angles between the Pb-X_n vectors and the **b** axis, a threefold periodicity was found (as expected): $\phi_n \sim (2n-1)\times 60° + \phi_0$, with $\max(|\phi_0|) = 1.2°$ for the fully iodinated species. Thus, the relative orientations of the octahedra are nearly identical in all four α-phases, and the uncommon anisotropic change of the lattice parameters cannot be attributed to progressively changing ϕ_0's. Finally, we found that these mixed halide structures maintain their average homogeneity on the long range, even after prolonged exposure to blue laser light (see Figure S4). On the contrary, hybrid 3D lead perovskites upon irradiation are reported to undergo a (reversible) detrimental phase change due to halide segregation[55].

Spectroscopic analysis

Infrared Spectroscopy. IR spectra are reported in Figure 8. All samples show the same vibrational bands in the 3700–1600 cm^{-1} range, which are essentially due to the PRS moieties. A slight blue-shift in the position of C–H stretching vibrations (2850–3000 cm^{-1} region) is observed between the x = 0–3 samples, amounting to around 4 cm^{-1} going from (PRSH)PbI_3 to (PRSH)$PbBr_3$. Even though they are isostructural, in (PRSH)$PbBr_3$ the cell volume (3844.2 $Å^3$) is 9% smaller than that in (PRSH)PbI_3 (4204.1 $Å^3$), so in the bromide compound the $PRSH^+$ ions are one closer to each other and to $[PbBr_3]_n^-$ chains, resulting in a stronger interaction between them. Pb–X stretching bands, on the other hand, only occur at very low

wavenumbers (less than 400 cm^{-1}), which are out of the range investigated here.

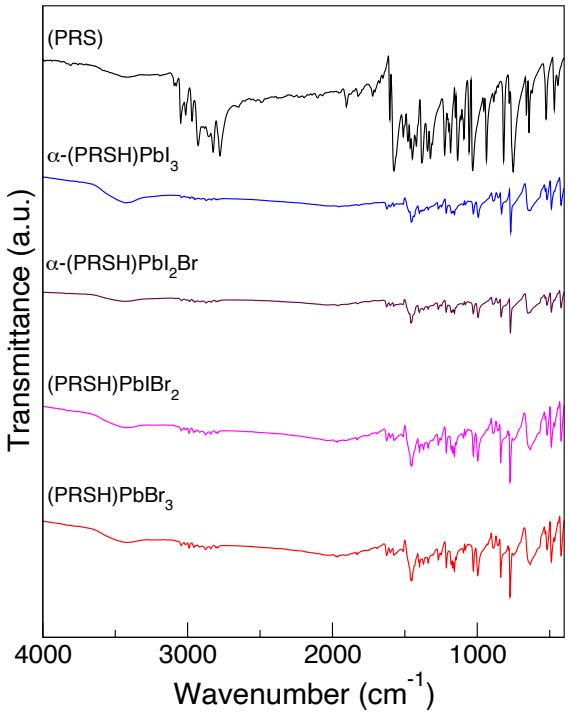

Fig. 8. IR spectra of PRS (black), α-(PRSH)PbI_3 (blue), (PRSH)PbI_2Br (brown), (PRSH)$PbIBr_2$ (magenta) and (PRSH)$PbBr_3$ (red).

Electronic properties. UV-vis diffuse reflectance data were analyzed to explore the electronic properties of the synthesized 1DHLHs. In the UV-vis spectra (Kubelka-Munk transformed, Figure 9) of the various samples, two different transitions can be seen in the range 2.8–3.8 eV; a similar behavior was recently reported for other 1DHLHs, where the higher energy transition was attributed to the proper band gap and the lower energy (and weaker) signal assigned to an excitonic (electron-hole interaction) band.[56] In our case, the band gap ranges from 3.25 to 3.75 eV for the α-(PRSH)PbX_3 (x = 0 – 3) samples (Figure 9a) and is shifted to higher energy with increasing bromide content. The $\alpha \rightarrow \beta$ phase transition does not influence the band gap, which therefore seems to be mainly dependent on the halide composition. The values are broadly comparable, even if slightly higher, to those found in other 1D structures, such as δ-$CsPbI_3$, δ-$FAPbI_3$, and $((CH_3)_3)SPbI_3$. The difference of about 0.5 eV observed between the iodide and bromide compositions is in line with what previously reported for 1DHLHs,[56] and also for 3D[57] and 2D[58] perovskites.

Thermodiffractometric Analysis

For both α-(PRSH)PbI_3, β-(PRSH)PbI_3 and (PRSH)$PbBr_3$ bulk samples, isolated in powdered form, the XRD patterns were also acquired from room temperature up to 250°C (Figure 11a and Figure S3), just below decomposition, measured by TG to occur above 270 °C (Figure S5). As expected from DSC measurements, β-(PRSH)PbI_3 and (PRSH)$PbBr_3$ only manifested a gradual thermal expansion, while, for α-(PRSH)PbI_3, the XRD pattern radically changed above 220 °C, as it transformed to β-(PRSH)PbI_3.

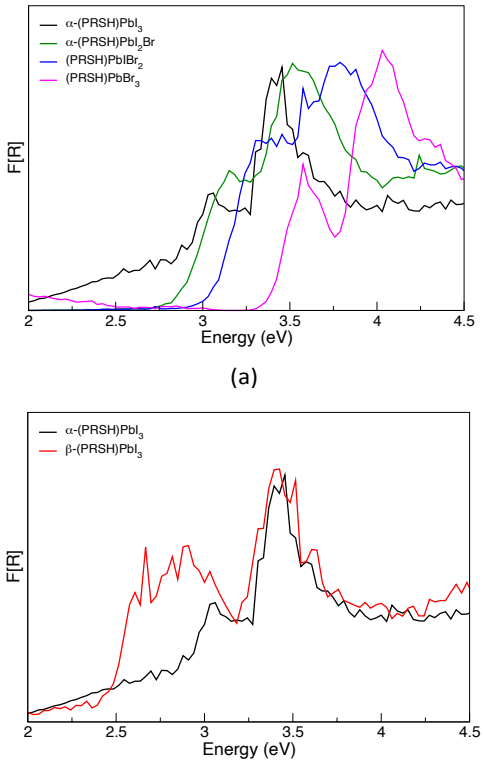

Fig. 9. UV-vis spectra (Kubelka-Munk transformed) of a) (α-)(PRSH)$PbI_{3-x}Br_x$ (x = 0–3) and b) of α– and β-(PRSH)PbI_3.

Highly anisotropic thermal expansion coefficients were determined using the cell parameters derived from structureless Le Bail fitting.[59] Using the linear approximation

$$p(T) = p(T_o)[1 + \kappa_p(T - T_o)] \qquad (2),$$

where p = a, b, c or V; T and T_0 are the actual and initial temperatures and κ_x are the pertinent linear (or volumetric) thermal expansion coefficients. The entire set of measured datapoints, expressed in the mathematically equivalent $\Delta p/p_{RT}$ = $\kappa_p \Delta T$, to whom linear regression was applied, are shown in Figure 10; the κ_p values and their uncertainties are reported in Table 3.

As clearly seen, in both α-(PRSH)PbI_3 and (PRSH)$PbBr_3$ crystal phases (Figure 10, panels a and c respectively), the a (blue markers) and c (grey dots) axes are basically unaffected by temperature changes, while the b parameter and, consequently, the cell volume, show κ_b and κ_V values in the 10^{-4} K^{-1} range, *i.e.* nearly two orders of magnitude larger than κ_a and κ_c (see Table 3). Such behavior is explained here by the progressive reorientation of the rigid organic cation, possibly through a rotation around a molecular axis parallel to **a**. Bearing in mind that the **c** length is constrained by the stiff

$([PbX_3]^-)_\infty$ chains, and that the rotation of the organic moiety would not significantly affect the **a** length, this leaves **b** as the only flexible direction.

The rather different crystal packing observed in the β-(PRSH)PbI_3, though iso-oriented with the α-polymorph, is also manifested by markedly different qualitative and quantitative trends, where the stiffer direction is no longer **c**, but **b**, and **a** becomes the most flexible direction (see Table 3).

The observation that the two α and β-(PRSH)PbI_3 phases show (at least) one direction with a large thermal expansion coefficient suggests also that their thermal response properties, such as thermal conductivity, possess a large anisotropy. This is, *inter alia*, a very interesting feature for 1DHLHs, as their possible use in thermoelectric devices requires, beyond film deposition and suitable crystal orientation, the lowering of the thermal conductivity, enhancing their thermoelectric figure of merit ZT. Counter-correlation between thermal expansion values and the lattice thermal conductivity was indeed experimentally proved for 3D lead halide perovskites.[60]

Table 3 reports a comparison between the thermal expansion coefficients (in MK^{-1}), κ_p (p =a,b,c,V) measured for the (PRSH)PbX_3 samples, and those found in the literature for other halide perovskites, either 1D or 3D. The values for linear expansion measured in the present study are high (on the order of 10^{-4} K^{-1}), exceptionally so if compared to other popular 1D pseudo-perovskites.

Table 3. Linear and volumetric thermal expansion coefficients (10^{-6} K^{-1}) of α-(PRSH)PbI_3, β-(PRSH)PbI_3 and (PRSH)$PbBr_3$. Reference values of other 3D and 1D perovskites are shown for comparison.

Composition		κ_a	κ_b	κ_c	κ_V
β-$MAPbI_3$ [61]	3D	132	$=\kappa_a$	−106	157
β-$FAPbI_3$ [62]	3D	77	$=\kappa_a$	49	206
δ-$FAPbI_3$ [63]	1D	67	$=\kappa_a$	*-2* [a]	130
δ-$CsPbI_3$ [64]	1D	39	*45*	29	113
α-(PRSH)PbI_3	1D	1(3)	112(1)	*12(3)*	125(5)
β-(PRSH)PbI_3	1D	84(1)	7(1)	*42(2)*	134(2)
(PRSH)$PbBr_3$	1D	7(1)	121(1)	*-3(1)*	125(1)

[a] Italicized values refer to the crystal axis associated to the lead halide chain directions

Structural Properties of Thin Films

The diffraction data of the (PRSH)PbI_3 thin film, measured at room temperature, show that it contains the α-(PRSH)PbI_3 phase, with significantly modified peaks intensities (see Figure 11a and b). The film shows enhanced intensities for the *h00* class of reflections, indicating that the **b** axis lies in the film plane, and not normal to it. This is an interesting feature, considering that **b** is the axis with the highest thermal expansion coefficient (and, likely, the lowest thermal conductivity – to be further investigated with dedicated experiments), and that the experimentally determined film orientation is the appropriate one for a cylindrically averaged film texture, if thermal conductivity must be minimized in the film plane. Similarly to the pristine powder sample, VTXRD data of the deposited film showed that the transformation to the β-phase occurs slightly above 200°C.

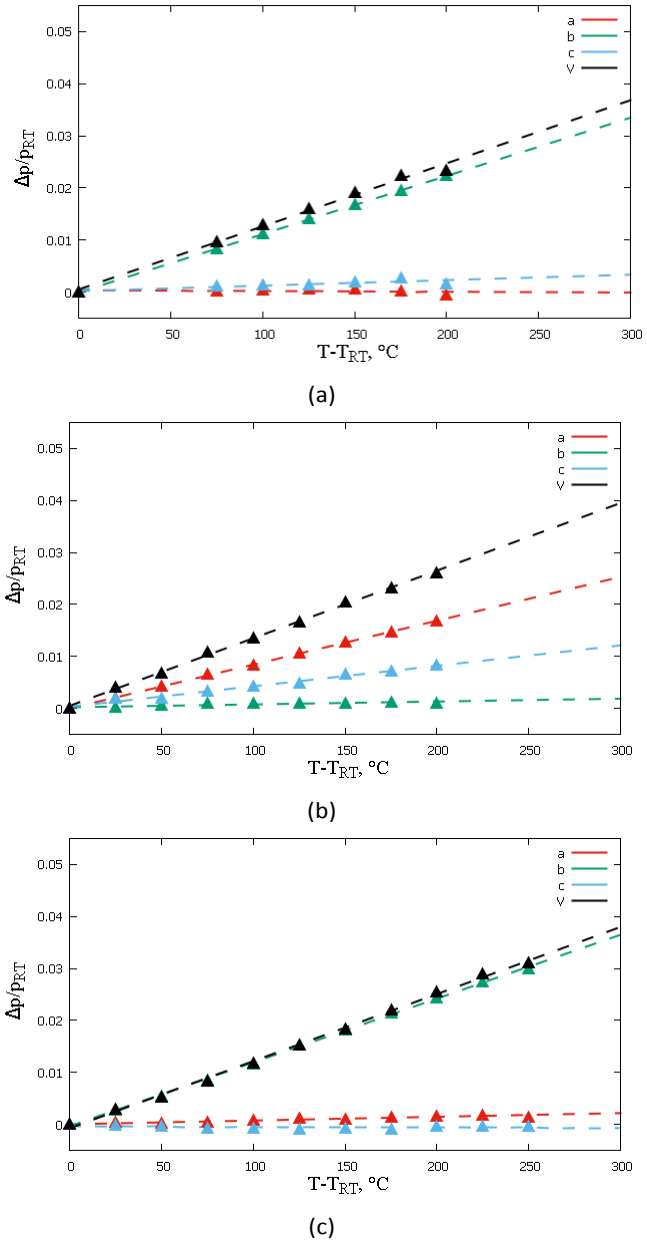

Fig. 10. Plot of the relative lattice parameter changes, in the form of $\Delta p/p_{RT}$ (p = a, b, c and V) vs. $\Delta T = T - 25°C$. The slope of these curves is the thermal expansion coefficient, κ_p, in the $x = x_{RT}(1+\kappa_p \Delta T)$ formulation. (a) α-(PRSH)PbI_3, (b) β-(PRSH)PbI_3, (c) (PRSH)$PbBr_3$.

Conclusions

In this paper, we report the synthesis as well as the crystal structure, thermal and spectroscopic analyses of new one-dimensional hybrid lead halides with general formula $(C_{14}H_{19}N_2)PbI_{3-x}Br_x$ (x = 0–3), precipitated from different (aqueous HI or DMF) media. Their crystal structures were determined using X-ray powder diffraction data acquired on polycrystalline samples. The strictly isomorphous iodine and bromine end members are mutually miscible, as a complete solid solution for any intermediate composition crystallizes, at

room temperature, in the orthorhombic *Pbca* space group with similar lattice parameters. In all these materials, infinite chains of $([PbX_3]^-)_\infty$ face-sharing octahedra are aligned with the **c** axis, which manifests the lowest variations upon anion substitution.

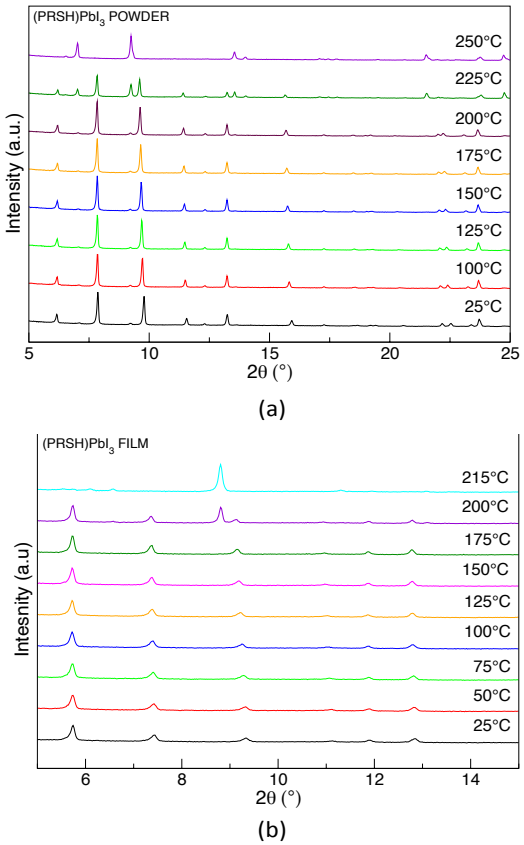

Fig, 11. VTXRD patterns of α-(PRSH)PbI_3 powder (a) and film (b), collected in the 25 – 250°C range, under isothermal conditions

The high-temperature behavior of these samples was investigated with variable-temperature XRPD, thermogravimetric and calorimetric analyses: in the case of α-(PRSH)PbI_3, a phase transition from *Pbca* to *Pca2₁* is observed around 220 °C. For all non-mixed phases, a very high linear thermal expansion coefficient (around 10^{-4} K^{-1}) is found in the crystallographic **b** direction. This is almost two times larger than what reported for 1D compounds, and more similar to 3D lead halide perovskites such as β-$MAPbI_3$. Highly textured thin films of the α-(PRSH)PbI_3 phase are obtained when deposited from the solution, with the **b** axis lying in the film plane.

Conflicts of interest

There are no conflicts to declare.

Acknowledgements

This project was partially supported by MIUR (PRIN-2017L8WW48, Project HY-TEC). We gratefully acknowledge Prof. F. Ferri (Università dell'Insubria), Dr. F. Armetta, Prof. G. Lazzara, and Prof. M.L. Saladino (Università di Palermo) for technical assistance and fruitful discussions. We thank Dr. G. Nasillo (Electron microscopy Lab, ATEN Center, Università di Palermo) for the SEM-EDS measurements. The courtesy of Prof. V. Colombo and Dr. T. Grell (University of Milano) is also acknowledged for measuring the single-crystal X-ray diffraction data.

Notes and references

1 P. Tonui, S. O. Oseni, G. Sharma, Q. Yan and G. Tessema Mola, *Renew. Sustain. Energy Rev.,* 2018, **91**, 1025
2 M. I. H. Ansari, A. Qurashi and M. K. Nazeeruddin, *J. Photochem. Photobiol. C Photochem. Rev,*. 2018, **35**, 1
3 M. A. Green, E. D. Dunlop, J. Hohl-Ebinger, M. Yoshita, N. Kopidakis and A. W. Y. Ho-Baillie, *Prog. Photovolt. Res. Appl.* 2020, **28**, 3
4 E. H. Jung, N. J. Jeon, E. Y. Park, C. S. Moon, T. J. Shin, T.-Y. Yang, J. H. Noh and J. Seo, *Nature,* 2019, **567**, 511
5 J. Zhang, W. Zhang, H.-M. Cheng and S. R. P. Silva, *Mater. Today,* 2020, **39**, 66
6 Research Cell Efficiency Chart. https://www.nrel.gov/pv/cell-efficiency.html (Accessed July 2020).
7 T. Kirchartz, J. A. Márquez, M. Stolterfoht and T. Unold, *Adv. Energy Mater.,* 2020, **10**, 1904134
8 A. Pisoni, J. Jaćimović, O. S. Barišić, M. Spina, R. Gaál, L. Forró and E. Horváth, *J. Phys. Chem. Lett.,* 2014, **5**, 2488
9 X. Mettan, R. Pisoni, P. Matus, A. Pisoni, J. Jaćimović, B. Náfrádi, M. Spina, D. Pavuna, L. Forró and E. Horváth, *J. Phys. Chem. C,* 2015**, 119**, 11506
10 T. Zhao, D. Wang and Z. Shuai, *Synth. Met.,* 2017, **225**, 108
11 Q. Chen, N. De Marco, Y. Yang, T.-B. Song, C.-C. Chen, H. Zhao, Z. Hong, H. Zhou and Y. Yang, *Nano Today,* 2015, **10**, 355
12 Y. Zhao and K. Zhu, *Chem. Soc. Rev.,* 2016, **45**, 655
13 A. Vassilakopoulou, D. Papadatos, I. Zakouras and I. Koutselas, *J. Alloys Compd.,* 2017, **692**, 589
14 M. Cheng, G. Li, H. Li, E. Xu, D. Li, H. Wang, F. Wu, H. Zhong and Y. Jiang, *J. Alloys Compd.* 2019, **791**, 814
15 L. Chen, J. Cai, J. Li, S.-P. Feng, G. Wei and W.-D. Li, *Org. Electron.,* 2019, **71**, 284
16 Z. Zhang, W. Zheng, R. Lin and F. Huang, *R. Soc. Open Sci.*, 2018, **5**, 180905
17 M. Stylianakis, T. Maksudov, A. Panagiotopoulos, G. Kakavelakis and K. Petridis, *Materials,* 2019, **12,** 859
18 L. Protesescu, S. Yakunin, S. Kumar, J. Bär, F. Bertolotti, N. Masciocchi, A. Guagliardi, M. Grotevent, I. Shorubalko, M. I. Bodnarchuk, C.-J. Shih and M. V. Kovalenko, *ACS Nano,* 2017, **11**, 3119
19 T. Krishnamoorthy, H. Ding, C. Yan, W. L. Leong, T. Baikie, Z. Zhang, M. Sherburne, S. Li, M. Asta, N. Mathews and S. G. Mhaisalkar, *J Mater Chem A,* 2015, **3,** 23829
20 C. C. Stoumpos, L. Frazer, D. J. Clark, Y. S. Kim, S. H. Rhim, A. J. Freeman, J. B. Ketterson, J. I. Jang and M. G. Kanatzidis, *J. Am. Chem. Soc.,* 2015, **137**, 6804
21 C. C. Stoumpos, C. D. Malliakas and M. G. Kanatzidis, *Inorg. Chem.,* 2013, **52**, 9019
22 D. Bryant, N. Aristidou, S. Pont, I. Sanchez-Molina, T. Chotchunangatchaval, S. Wheeler, J. R. Durrant and S. A. Haque, *Energy Environ. Sci.*, 2016, **9**, 1655
23 S. He, L. Qiu, L. K. Ono and Y. Qi, *Mater. Sci. Eng. R Rep.,* 2020, **140**, 100545

24 G. Kieslich, S. Sun and A. K. Cheetham, *Chem. Sci.,* 2015, **6**, 3430
25 R. Ali, G.-J. Hou, Z.-G. Zhu, Q.-B. Yan, Q.-R. Zheng and G. Su, *Chem. Mater.,* 2018, **30**, 718
26 P. P. Boix, S. Agarwala, T. M. Koh, N. Mathews and S. G. Mhaisalkar, *J. Phys. Chem. Lett.,* 2015, **6**, 898
27 B. Saparov and D. B. Mitzi, *Chem. Rev.,* 2016, **116**, 4558
28 M. Aebli, B. Benin, K. M. McCall, M. Viktoriia, D. Thöny, H. Grützmacher and M. V. Kovalenko, *Helv. Chim. Acta,* 2020, **102**, e20000080
29 K. Wang, Z. Jin, L. Liang, H. Bian, D. Bai, H. Wang, J. Zhang, Q. Wang and S. Liu, *Nat. Commun.,* 2018, **9**, 4544
30 Y. Zhang, Z. Zhou, F. Ji, Z. Li, G. Cui, P. Gao, E. Oveisi, M. K. Nazeeruddin and S. Pang, *Adv. Mater.,* 2018, **30**, 1707143
31 M. M. Elsenety, M. Antoniadou, N. Balis, A. Kaltzoglou, L. Sygellou, A. Stergiou, N. Tagmatarchis and P. Falaras, *ACS Appl. Energy Mater.,* 2020, **3**, 2465
32 Q. Yao, Q. Xue, Z. Li, K. Zhang, T. Zhang, N. Li, S. Yang, C. J. Brabec, H. Yip and Y. Cao, *Adv. Mater.,* 2020, **32**, 2000571
33 P. Zhu and J. Zhu, *InfoMat,* 2020, **2**, 341
34 T. T. Ava, A. Al Mamun, S. Marsillac and G. Namkoong, *Appl. Sci.,* 2019, **9**, 188
35 Y. Fan, H. Meng, L. Wang and S. Pang, *Sol. RRL*, 2019, **3**, 1900215
36 V. L. Pool, B. Dou, D. G. Van Campen, T. R. Klein-Stockert, F. S. Barnes, S. E. Shaheen, M. I. Ahmad, M. F. A. M. van Hest and M. F. Toney, *Nat. Commun.* 2017, **8**, 14075
37 A. A. Coelho, *J. Appl. Crystallogr.* 2003, **36**, 86
38 TOPAS_R, v.3.0, 2005, Bruker AXS, Karlsruhe, Germany.
39 R. W. Cheary and A. Coelho, *J. Appl. Crystallogr.*, 1992, **25**, 109
40 W. A. Dollase, *J. Appl. Crystallogr.,* 1986, **19**, 267
41 P. Kubelka and F.Munk, *In- Zeit. Für Tekn. Physik*, 1931, **12**, S. 593
42 A. A. Petrov, N. Pellet, J.-Y. Seo, N. A. Belich, D. Yu. Kovalev, A. V. Shevelkov, E. A. Goodilin, S. M. Zakeeruddin, A. B. Tarasov and M. Graetzel, *Chem. Mater.,* 2017, **29**, 587
43 A. A. Petrov, I. P. Sokolova, N. A. Belich, G. S. Peters, P. V. Dorovatovskii, Y. V. Zubavichus, V. N. Khrustalev, A. V. Petrov, M. Grätzel, E. A. Goodilin and A. B. Tarasov, *J. Phys. Chem. C,* 2017, **121**, 20739
44 R. D. Shannon, *Acta Cryst.,* 1976, **A32**, 751
45 A. Lemmerer and D. G. Billing, *Acta Crystallogr.,* 2006, **E62**, m904
46 A. Burger and R. Ramberger, *Mikrochim. Acta,* 1979, **72**, 273
47 G. Perlovich and A. Surov, *Acta Cryst.,* 2020, **B76**, 65
48 Y. Yoshida, J. Hatori, H. Kawakami, Y. Matsuo and S. Ikehata, *Symmetry,* 2012, **4**, 507
49 G. L. Murphy, C.-H. Wang, G. Beridze, Z. Zhang, J. A. Kimpton, M. Avdeev, P. M. Kowalski and B. J. Kennedy, *Inorg. Chem.,* 2018, **57**, 5948
50 S. K. Filatov, *Crystallogr. Rep.,* 2011, **56**, 953
51 R. Yu, E. S. Bozin, M. Abeykoon, B. Sangiorgio, N. A. Spaldin, C. D. Malliakas, M. G. Kanatzidis and S. J. L. Billinge, *Phys. Rev. B,* 2018, **98**, 144108
52 STRAIN by Ohashi, Y. (1982) A Program to Calculate the Strain Tensor from Two Sets of Unit-Cell Parameters. In Hazen, R. M. and Finger, L. W., Comparative Crystal Chemistry. NY, Wiley, Pp. 92-102.
53 WinTensor, Tensor-Drawing and Calculation Tool for Windows 9598NT2000XP. University of Washington, Seattle, USA.
54 E. Zen, *Am. Mineral.,* 1956, **41**, 523
55 M. C. Brennan, S. Draguta, P. V. Kamat and M. Kuno, *ACS Energy Lett.* 2018, **3**, 204
56 A. Kaltzoglou, M. M. Elsenety, I. Koutselas, A. G. Kontos, K. Papadopoulos, V. Psycharis, C. P. Raptopoulou, D. Perganti, T. Stergiopoulos and P. Falaras, *Polyhedron,* 2018, **140**, 67
57 L. Dimesso, M. Dimamay, M. Hamburger, W. Jaegermann, *Chem. Mater.,* 2014, **26**, 6762
58 M. E. Madjet, G. R. Berdiyorov and S. Ashhab, *Comput. Mater. Sci.,* 2019, **169**, 109130
59 A. Le Bail, *Powder Diffr.,* 2005, **20**, 316
60 M. A. Haque, S. Kee, D. R. Villalva, W. Ong and D. Baran, *Adv. Sci.,* 2020, **7**, 1903389
61 T. J. Jacobsson, L. J. Schwan, M. Ottosson, A. Hagfeldt and T. Edvinsson, *Inorg. Chem.,* 2015, **54**, 10678
62 D. H. Fabini, C. C. Stoumpos, G. Laurita, A. Kaltzoglou, A. G. Kontos, P. Falaras, M. G. Kanatzidis and R. Seshadri, *Angew. Chem. Int. Ed*., 2016, **55**, 15392
63 M. Keshavarz, M. Ottesen, S. Wiedmann, M. Wharmby, R. Küchler, H. Yuan, E. Debroye, J. A. Steele, J. Martens, N. E. Hussey, M. Bremholm, M. B. J. Roeffaers and J. Hofkens, *Adv. Mater.,* 2019, **31**, 1900521
64 T. Burwig, W. Fränzel and P. Pistor, *J. Phys. Chem. Lett.,* 2018, **9**, 4808